RESEARCH ARTICLE

Analysis of damage and failure behavior of additively manufactured stainless steel 316L by biaxial experiments

Steffen Gerke[1] | **Johannes Diller**[2] | **Leonardo D. Pérez Cruz**[1,3] | **Jakob Blankenhagen**[2] | **Martin Mensinger**[2] | **Michael Brünig**[1]

[1]Institut für Mechanik und Statik, Universität der Bundeswehr München, Neubiberg, Germany

[2]Lehrstuhl für Metallbau, Technische Universität München (TUM), Munich, Germany

[3]Facultad de Ingenería, Universidad Nacional de Mar del Plata, Mar del Plata, Argentina

Correspondence
Steffen Gerke, Institut für Mechanik und Statik, Universität der Bundeswehr München, 85579 Neubiberg, Germany.
Email: steffen.gerke@unibw.de

Abstract

The austenitic stainless steel AISI 316L (1.4404) is frequently used in medical applications as well as in aerospace and automotive industries due to its corrosion resistance and high ductility. Individual parts or smaller series as well as complex geometries can be additively manufactured by laser powder bed fusion (PBF-LB/M). The components produced in this process generally have different mechanical properties compared to components made from conventionally produced base material by cutting machining processes. Furthermore, the multiaxial stress state behavior of PBF-LB/M/316L has not been investigated in detail and is the subject of current investigations. This paper deals with an initial experimental series with additively manufactured biaxial specimens made of AISI 316L stainless steel. The biaxial specimen geometry has been specially adapted for the requirements of PBF-LB/M and the specimens are loaded under different biaxial proportional load paths up to failure. Accompanying numerical simulations are performed to determine the associated stress states and to analyze the experimentally obtained stress-dependent damage and failure mechanisms. The formation of strain fields in critical parts of the modified H-specimen is monitored by digital image correlation and the different failure modes are visualized by scanning electron microscopy of the fracture surfaces.

1 | INTRODUCTION

The additive manufacturing of metals is experiencing strong growth and the underlying technology is making continuous progress, so that in future it can be expected to produce reliable individual parts and small series in this way. Powder bed based laser melting (PBF-LB/M) is particularly attractive and there is a need for detailed investigations into the material behavior since properties cannot be transferred directly from conventionally produced ones. Numerous studies have investigated the influence on the mechanical properties of PBF-LB/M/316L [1–3], wherein the influence of the build-up direction in particular became clear and can be traced back to the microstructure of the material [4]. The laser beam, which is responsible for melting the metal powder during the manufacturing process, is always radiated onto the powder bed from above. Grain nucleation begins at the bottom of the melting bath, with subsequent grain growth occurring predominantly in the direction of deposition, which is aligned with the thermal gradient. As a result, different cell diameters

TABLE 1 Applied laser parameters for specimen manufacturing.

Energy density (J/mm^3)	Laser power (W)	Scan velocity (mm/s)	Hatch distance (mm)	Layer thickness (mm)
65.00	192	750	0.1	0.04

are observed at different grain locations. These discrepancies result from the angle at which the dendrites intersect the image plane, as well as from the specific thermal gradient and the solidification rate of the melt pool. Consequently, the dendrite orientation primarily reflects the direction of the thermal gradient [4]. This orientation of the grains in turn varies depending on the hatching strategy. Thus, additively manufactured components have a significantly different microstructure, therefore resulting in different mechanical properties compared to sheet metal that has been rolled, although the chemical composition shows only slight differences [5]. Additively manufactured 316L has a significantly higher yield stress with less strain hardening compared to conventionally manufactured 316L. The ductile damage behavior, which is strongly dependent on the stress state, has not yet been investigated for additively manufactured 316L stainless steel.

The analysis of the damage and failure behavior is a major challenge, where the shape of the specimens used and the associated test facilities have a significant influence on the stress state prevailing in the damage area. Initial investigations for conventional sheet metal were carried out with notched or otherwise modified shoulder specimens [6–8], which indicate stress triaxialities between 0.33 and 0.7 with considerable gradients. Shear stress states with stress triaxialities around 0 can be obtained with specially designed, one-dimensionally loaded specimens [7, 9, 10]. However, a superposition of these two stress states is difficult to realize in standard testing machines. One approach is to use butterfly-shaped specimens, which can be loaded in different directions [11–13], but they are very complex to manufacture from sheet metal. Another possibility to adjust different stress states seems to be biaxial test specimens with a homogeneous central zone. Unfortunately this type of specimens localize at more elevated strains and uncontrolled failure occurs [14]. Furthermore, new biaxial test specimens with a central opening and pre-notches [15, 16] enable the generation of different stress states by means of different load ratios and allow the detailed analysis of damage and failure behavior. These test specimens were successfully used under various proportional and non-proportional loads to quantify the damage and failure behavior [17, 18].

The first study presented here combines the investigation of the damage and failure behavior of additively manufactured components made of 316L stainless steel with biaxially loaded specimens. An initial series of experiments is carried out and evaluated under various loading conditions. For this purpose, the geometry of the H-specimen, see for example, ref. [18], had to be adapted to allow production in the building space of the powder bed fusion machine. The evaluation is based on global load-displacement curves, by strain fields in critical region of the specimen obtained by digital image correlation (DIC) and by scanning electron microscope (SEM) images of the fracture surface. These images in particular show that the fracture patterns exhibit a greatly altered topology based on the loading condition.

2 | MATERIAL, EXPERIMENTAL SETUP AND SPECIMEN DESIGN

Powder made of stainless steel 316L (1.4404) supplied by Oerlikon Metco was used to produce the biaxial test specimens. The fabrication was carried out using an EOS M280 PBF-LB/M production cell equipped with a 400 W ytterbium continuous wave fiber laser. The metal powder used had a particle size distribution of $20 - 63\mu m$, with the respective volume percentile values of D10, D50, and D90 measured at 19, 30, and $46\mu m$. The manufacturing process took place under Argon 5.0 gas atmosphere, in which the residual oxygen concentration was below 1300 ppm in the build chamber. Furthermore, the heating temperature of the build platform was set to 80°C. The scan strategy was carried out with an x-rotation with an angle change of 60° after each layer, where the specific laser parameters used can be found in Table 1.

To gain initial insights into the stress state, which is represented here by the stress triaxiality

$$\eta = \frac{\sigma_m}{\sigma_{eq}} \tag{1}$$

with mean stress σ_m and the von Mises equivalent stress σ_{eq} and the Lode parameter expressed in terms of the principal stresses T_i

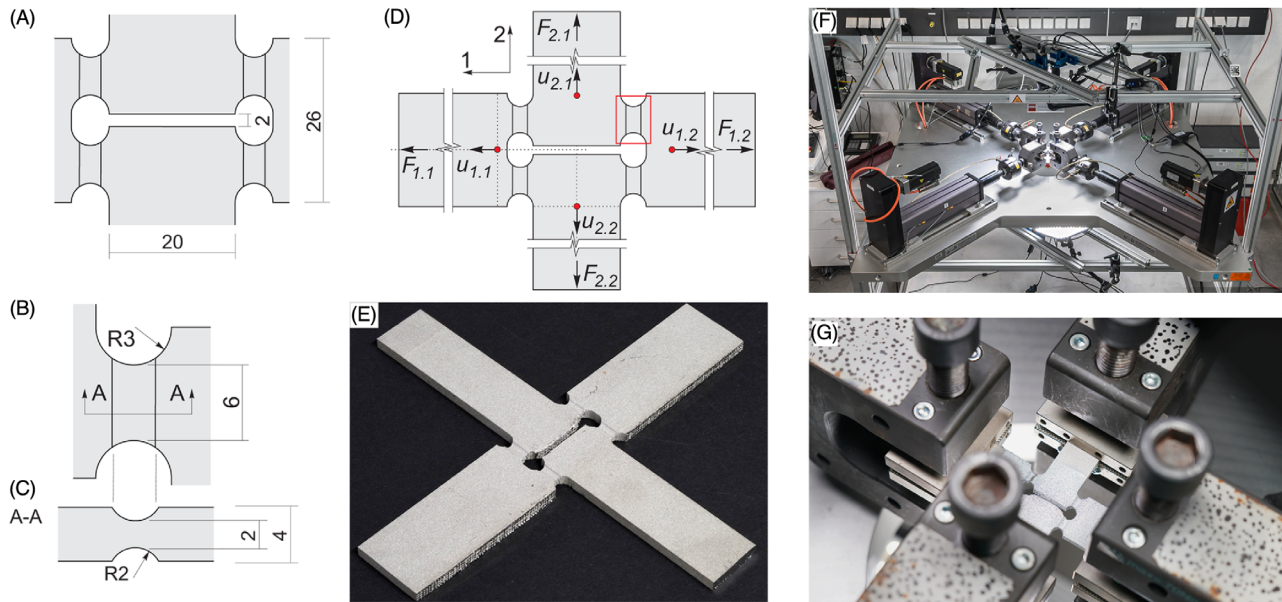$$\omega = \frac{2T_2 - T_1 - T_3}{T_1 - T_3} \quad \text{with} \quad T_1 \geq T_2 \geq T_3, \tag{2}$$

FIGURE 1 Specimen geometry, notation and experimental setup: (A) detail of central part, (B), (C) detail notch, (E) Photo of complete specimen, (D) notation, (F) DIC and machine setup, (G) clamping; all measures in (mm). DIC, digital image correlation.

accompanying elastic-plastic numerical simulations were carried out with Ansys. The elastic behavior is characterized by the Young's modulus $E = 140\,000\,{}^N/mm^2$ and Poisson's ratio $\nu = 0.3$. The plastic behavior is based for these first simulations on non-linear isotropic hardening (`nliso`) with the Voce hardening law

$$c = k + R_0 \varepsilon^{pl} + R_\infty \left(1 - e^{-b\varepsilon^{pl}}\right). \tag{3}$$

The associated material parameters have been chosen to $k = 436\,{}^N/mm^2$, $R_0 = 740\,{}^N/mm^2$, $R_\infty = 165\,{}^N/mm^2$ and $b = 80$.

On the one hand, the limited space of the production cell for powder bed fusion of the EOS M280 PBF-LB/M when manufacturing the biaxial test specimens must be complied with. On the other hand, the minimum specimens size for the biaxial testing in the electromechanical machine LFM-BIAX 20 kN from Walter & Bai must also be respected including sufficient clamping length, especially under compressive loading where clamping jaws move towards each other. Figure 1A gives an overview of the test setup and Figure 1B shows the remaining tight distances between the clamping jaws for the selected specimen size of $150 \times 150\,mm^2$. The H-specimen with reduced outer dimensions is used (Figure 1A–C,E), which was additively manufactured upright with notches perpendicular to the base plate. The evaluation of the displacements and strains of the specimen surface is carried out using DIC, using a system from Dantec/Limess, see Figure 1B. Details on the specimen geometry, test setup, test execution and evaluation can be found in previous publications, see for example, refs. [16, 17]. The associated notation, in particular the designation of the directions, is shown in Figure 1D. The sum of the respective displacements of the red points in the respective axis direction were selected as appropriate displacement measures

$$\Delta u_{\text{ref}.i} = u_{i.1} + u_{i.2}, \tag{4}$$

see Figure 1D, and the mean force in each axis

$$F_i = \frac{F_{i.1} + F_{i.2}}{2} \tag{5}$$

as the corresponding force quantity.

3 | RESULTS

In the experimental series presented here, a broad range of possible stress states is covered to analyze the stress state dependent damage and failure behavior of the additively manufactured stainless steel AISI 316L. The numerically cal-

TABLE 2   Averaged values to characterize the stress state at 70% maximum displacement.

F_2/F_1	1/0	0/1	−1/1	1/1
Stress triaxiality η	0.67	0.13	−0.08	0.34
Lode parameter ω	−0.44	−0.30	0.12	−0.78
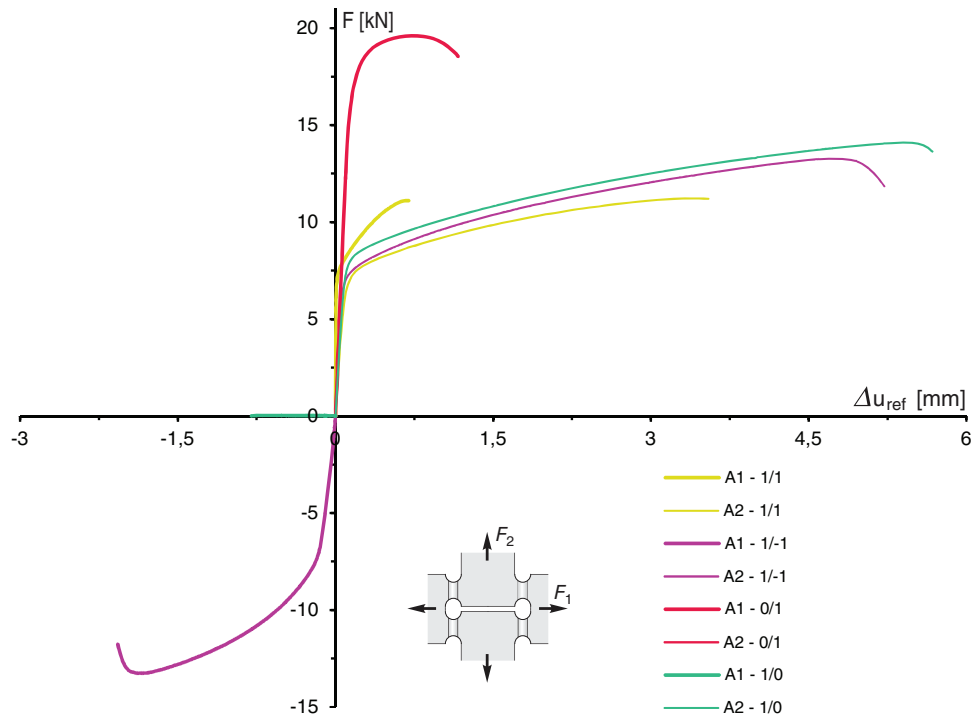
FIGURE 2   Experimentaly obtained load-displacement-curves of the different load cases, $\Delta u_{\text{ref},i}$ and F_i are defined in Equation (4) and Equation (5), furthermore see Figure 1D.

culated stress state averaged over the notch cross-section is given in Table 2 in which the two basic load cases provide significantly different stress states: Tensile load in axis 1 (see Figure 1D, $F_2/F_1 = 0/1$) provides tension-dominant stress states with $\eta = 0.67$ and $\omega = -0.44$, which are reinforced by the double-notched geometry and, in contrast, tensile loading in axis 2 ($F_2/F_1 = 1/0$) provides shear-dominant stresses with $\eta = 0.13$ and $\omega = -0.30$. In addition, shear superimposed by compression ($F_2/F_1 = -1/-1$) and superimposed by tension ($F_2/F_1 = -1/1$) is also considered. Thus, in this first experimental series, stress triaxialities in the range from $\eta = -0.08$ to 0.67 were covered.

The global deformation behavior based on load-displacement curves is shown for the four load cases in Figure 2. The load case $F_2/F_1 = 0/1$, that is, only tensile loading in axis 1 (A1) reaches by far the highest load with $F_1 = 19.2$ kN, wherein there is, compared to the other load cases, a rather small relative displacement $\Delta u_{\text{ref},1} = 1.2$ mm. In axis 2 ($F_2 = 0$ kN) there are almost no displacements. Under shear loading (1/0), forces up to $F_2 = 12.5$ kN occur and the associated maximum relative displacement $\Delta u_{\text{ref},2} = 5.1$ mm is significantly higher than in the load case 0/1. In the unloaded axis 1, displacements up to $u_{\text{ref},1} = 0.65$ mm occur here. The other load cases (1/−1 and 1/1) achieve slightly lower maximum loads than in the load case 1/0, where greater relative displacements are observed under superimposed compression 1/−1 than under superimposed tension 1/1.

The surface strains in the notch region, which were determined using DIC, are shown in Figure 3 at 70% of the maximum displacement. The distributions of the first and second principal strains are displayed for the notch boxed in red in Figure 1D and the final fracture is also shown for this notch in Figure 4. Furthermore, Figure 5 indicates the texture of the fracture surfaces taken by scanning electron microscopy (SEM). Under tensile loading in axis 1 (0/1), a rather wide area of elevated first principal strain appears on the surface (Figure 3A), where increased negative values of the second principal strain occur towards the notch boundaries (Figure 3E). Accordingly, the fracture line is rather irregular (Figure 4A) with characteristics of the typical "cup-and-cone" behavior. On the fracture surface Figure 5A, pores with remarkable
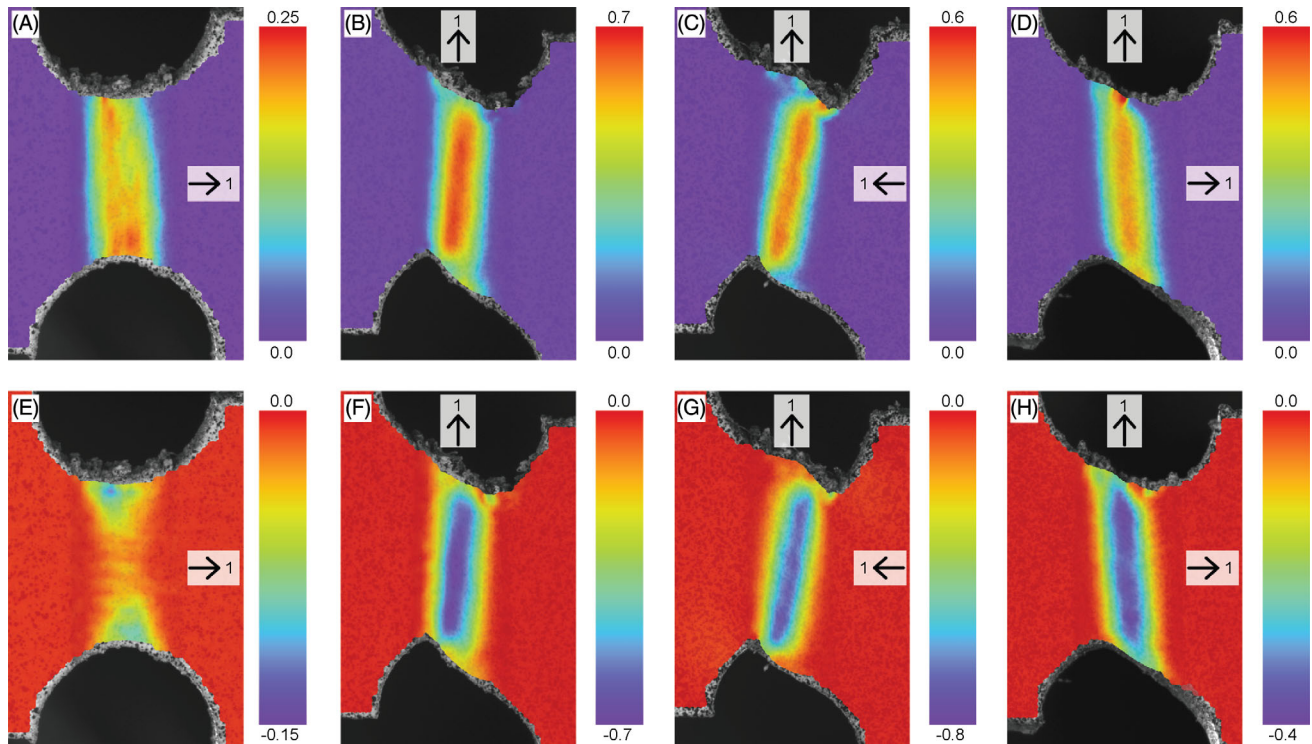
FIGURE 3 First (A)–(D) and second (E)–(H) principal strain at 70% of maximum displacement: (A)–(E) $F_2/F_1 = 0/1$, (B), (F) 1/0, (C), (G) $1/-1$ and (D), (H) 1/1.

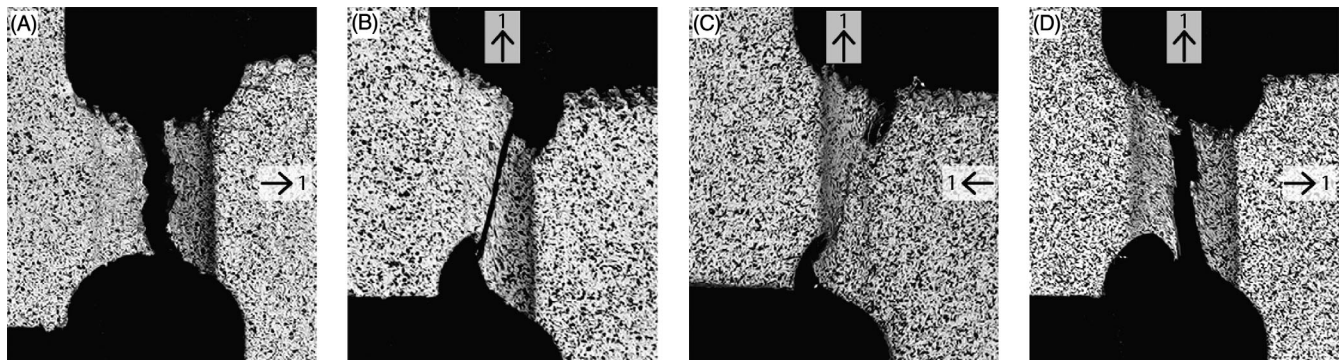**FIGURE 4** Fractured specimens: (A) $F_2/F_1 = 0/1$, (B) 1/0, (C) $1/-1$, and (D) 1/1.

diameters can be clearly seen as a result of the growth typical of this stress triaxiality. Under tensile loading in axis 2 (1/0), which results in shear stresses in the notch region, the formation of a shear band with associated maximum principal strains of 0.7 and −0.7 is clearly visible (Figure 3C,F), in which the crack also follows this shear band, compare Figure 4B. The fracture surface (Figure 5B) is comparatively smooth and has no significant pores. The results of the tests under tensile superimposed shear loading 1/1 (Figures 3D,H, 4D, and 5D) with an average triaxiality of $\eta = 0.3$ show a shear band and a smooth fracture line, while the fracture surface reflects pore formation and shear cracks, and consequently, characteristics of the experiments 1/0 and 0/1 are reflected. The experiment with compression superimposed shear loading −1/1 (Figures 3C,G, 4C, and 5C) has more elevated absolute second principal strains than the first principal strains, reflecting the compression loading in axis 1. Furthermore, the fracture line as well as the fracture surface reflects these loading conditions.
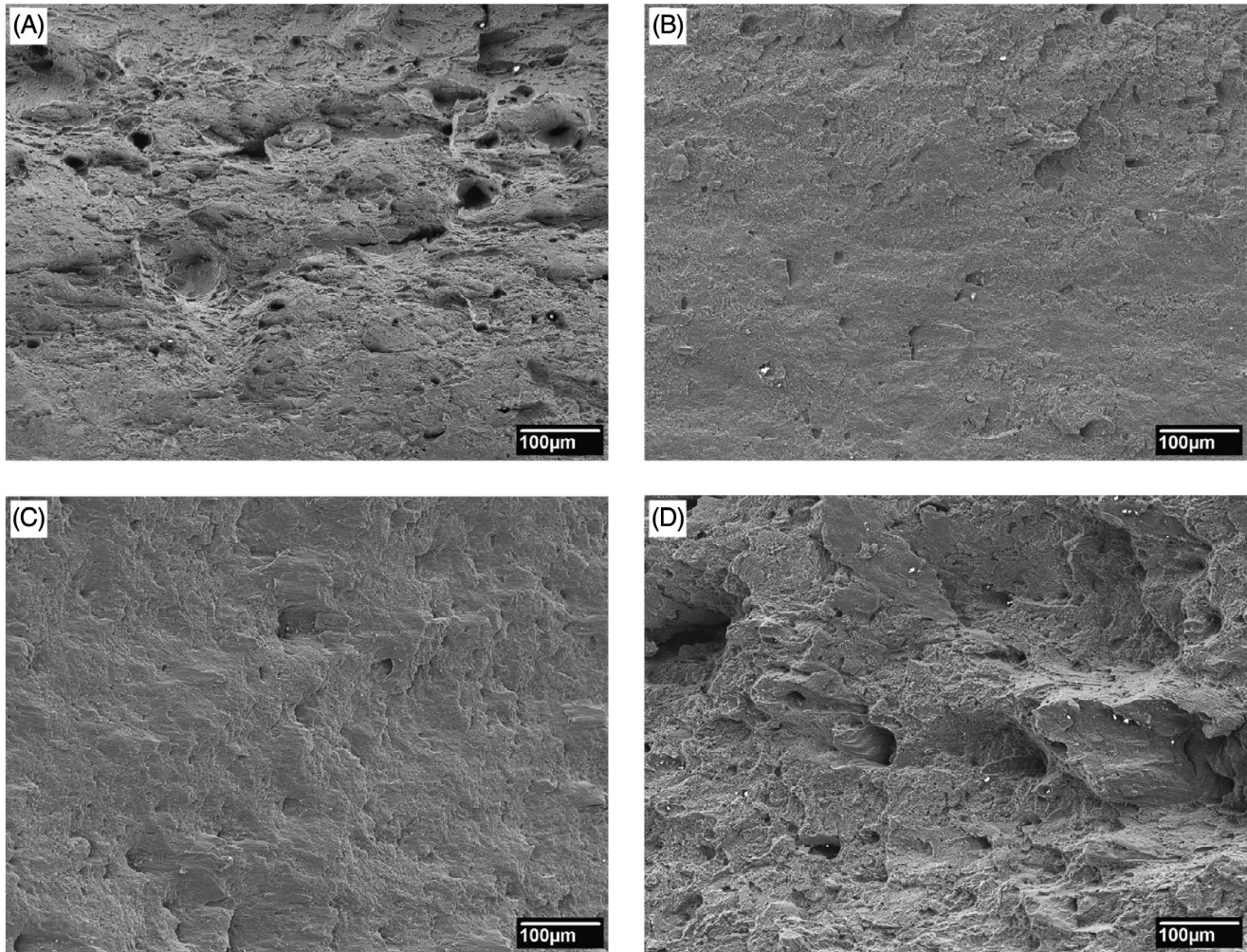
FIGURE 5 Scanning electron microscopy (SEM) images with magnification 150: (A) $F_2/F_1 = 0/1$, (B) 1/0, (C) 1/ − 1, and (D) 1/1.

4 | CONCLUSIONS

The experimental setup as well as the H-specimen geometry could be modified successfully to realize a first experimental series under biaxial loading with additively manufactured 316L stainless steel. This series indicates clearly that the damage and failure behavior of additively manufactured 316L stainless steel depends strongly on the stress state. For this purpose, a wide range of loading conditions has been applied and the deformation behavior and fracture surfaces have been analyzed. The main findings can be summarized as follows:

- The reduced H-specimen presented here enables the targeted analysis of the damage and failure behavior of additively manufactured metals.
- The additively manufactured specimens could be used directly without further post-processing by cutting machining.
- The fracture surfaces indicate a more pronounced void growth under tensile stress states than in those of conventional sheets. This is possibly due to the different microstructure resulting from additive manufacturing.

In the future, a suitable damage and failure model must be developed for this additively manufactured material, taking into account the anisotropic material behavior. In addition, an extensive experimental program has to be realized to illuminate particularly the damage and failure behavior. Furthermore, in the experimental program it can be considered that additive manufacturing enables the development of more complex biaxial specimen geometries.

ACKNOWLEDGMENTS

ORCID

Steffen Gerke https://orcid.org/0000-0003-2261-3855

REFERENCES

1. DebRoy, T., Wei, H. L., Zuback, J. S., Mukherjee, T., Elmer, J. W., Milewski, J. O., Beese, A. M., Wilson-Heid, A., De, A., & Zhang, W. (2018). Additive manufacturing of metallic components – Process, structure and properties. *Progress in Materials Science*, *92*, 112–224.
2. Lewandowski, J. J., & Seifi, M. (2016). Metal additive manufacturing: A review of mechanical properties. *Annual Review of Materials Research*, *46*(1), 151–186.
3. van Nuland, T. F. W., van Dommelen, J. A. W., & Geers, M. G. D. (2021). Microstructural modeling of anisotropic plasticity in large scale additively manufactured 316L stainless steel. *Mechanics of Materials*, *153*, 103664.
4. Godec, M., Sinko, M., & Tchernychova, E. (2020). Quantitative multiscale correlative microstructure analysis of additive manufacturing of stainless steel 316L processed by selective laser melting. *Materials Characterization*, *160*, 110074.
5. Diller, J., Siebert, D., Radlbeck, C., & Mensinger, M. (2022). PBF-LB/M/316L vs. hot-rolled 316L – Comparison of cyclic plastic material behavior. *Procedia Structural Integrity*, *42*(12), 58–65.
6. Bonora, N., Gentile, D., Pirondi, A., & Newaz, G. (2005). Ductile damage evolution under triaxial state of stress: theory and experiments. *International Journal of Plasticity*, *21*(5), 981–1007.
7. Brünig, M., Chyra, O., Albrecht, D., Driemeier, L., & Alves, M. (2008). A ductile damage criterion at various stress triaxialities. *International Journal of Plasticity*, *24*(10), 1731–1755.
8. Gao, X., Zhang, G., & Roe, C. (2010). A study on the effect of the stress state on ductile fracture. *International Journal of Damage Mechanics*, *19*(1), 75–94.
9. Roth, C. C., & Mohr, D. (2016). Ductile fracture experiments with locally proportional loading histories. *International Journal of Plasticity*, *79*, 328–354.
10. Wei, Z., Zistl, M., Gerke, S., & Brünig, M. (2022). Analysis of ductile damage and fracture under reverse loading. *International Journal of Mechanical Sciences*, *228*, 107476.
11. Mohr, D., & Henn, S. (2007). Calibration of stress-triaxiality dependent crack formation criteria: A new hybrid experimental–numerical method. *Experimental Mechanics*, *47*(6), 805–820.
12. Dunand, M., & Mohr, D. (2011). On the predictive capabilities of the shear modified Gurson and the modified Mohr–Coulomb fracture models over a wide range of stress triaxialities and Lode angles. *Journal of the Mechanics and Physics of Solids*, *59*(7), 1374–1394.
13. Wilson-Heid, A. E., Qin, S., & Beese, A. M. (2020). Multiaxial plasticity and fracture behavior of stainless steel 316L by laser powder bed fusion: Experiments and computational modeling. *Acta Materialia*, *199*, 578–592.
14. Kuwabara, T. (2007). Advances in experiments on metal sheets and tubes in support of constitutive modeling and forming simulations. *International Journal of Plasticity*, *23*(3), 385–419.
15. Gerke, S., Adulyasak, P., & Brünig, M. (2017). New biaxially loaded specimens for the analysis of damage and fracture in sheet metals. *International Journal of Solids and Structures*, *110-111*, 209–218.
16. Gerke, S., Zistl, M., Bhardwaj, A., & Brünig, M. (2019). Experiments with the X0-specimen on the effect of non-proportional loading paths on damage and fracture mechanisms in aluminum alloys. *International Journal of Solids and Structures*, *163*, 157–169.
17. Brünig, M., Gerke, S., & Zistl, M. (2019). Experiments and numerical simulations with the H-specimen on damage and fracture of ductile metals under non-proportional loading paths. *Engineering Fracture Mechanics*, *217*, 106531.
18. Brünig, M., Koirala, S., & Gerke, S. (2022). Analysis of damage and failure in anisotropic ductile metals based on biaxial experiments with the H-specimen. *Experimental Mechanics*, *62*, 183–197.